Study on three dimensional morphogenesis of epithelial cells on the viscous substrata: Involvement of substrate deformation induced by cellular traction forces

(培養基質の粘性が上皮細胞集団の 3 次元形態形成に与える影響に関する研究：

基質把握力による培養基質の変形の関与)

Misako Imai

2015

Doctoral Dissertation

Transdisciplinary Life Science Course

Graduate School of Life Science

Hokkaido University

Contents

Abbreviations

1P-MRLC: mono-phosphorylated MRLC

2P-MRLC: di-phosphorylated MRLC

ECM: extracellular matrix

GP: genipin

GP-Matrigel: genipin-treated matrigel

MDCK: Madin-Darby Canine Kidney

MELC: myosin essential light chain

MHC: myosin heavy chain

MRCK: myosin II light chain kinase

MRLC: myosin II regulatory light chain

NT-Matrigel: non-treated matrigel

P-MRLCs: mono-phosphorylated and di-phosphorylated MRLC

Rho-kinase: Rho-associated coiled-coil forming protein kinase

Abstract

Substrate physical properties are essential for many physiological events such as embryonic development and 3D tissue formation. Physical properties of the extracellular matrix such as viscoelasticity and geometrical constraints are understood as factors that affect cell behaviour. In this study, we focused on the relationship between epithelial cell 3D morphogenesis and the substrate viscosity. We observed that Madin-Darby Canine Kidney (MDCK) cells formed 3D structures on a viscous substrate (Matrigel). The structures appear as a tulip hat. We then changed the substrate viscosity by genipin (GP) treatment. GP is a cross-linker of amino groups. Cells cultured on GP-treated-matrigel changed their 3D morphology in a substrate viscosity-dependent manner. Furthermore, to elucidate the spatial distribution of the cellular traction force, localization of mono-phosphorylated and di-phosphorylated myosin II regulatory light chain (P-MRLCs) was visualized by immunofluorescence. P-MRLCs localized along the periphery of epithelial sheets. Treatment with Y-27632, a Rho-kinase inhibitor, blocked the P-MRLCs localization at the edge of epithelial sheets and halted 3D morphogenesis. Our results indicate that the substrate viscosity, the substrate deformation, and the cellular traction forces induced by P-MRLCs play crucial roles in 3D morphogenesis.

Chapter 1

Introduction

1.1 3D morphogenesis of epithelial cells in physiological phenomena

3D morphogenesis is an essential process for various *in vivo* phenomena such as embryonic development and tissue formation. Various tissues such as intestinal villus, brain sulcus are composed of epithelial sheets that hollow and form concavo-convex structures.

Length of apical and basolateral surfaces needs to regulate for formation of concavo-convex epithelial sheets. Individual cell shape in the epithelial sheets is controlled by external and endogenous signal[1,2]. For instance, RhoA and Rac1 activity regulates the cell shape in the epithelial sheet during lens placode invagination[1] (Figure 1-1). In the apical surface, shrinkage of apical surface was induced by RhoA activity, whereas activity of Rac1 involved in elongation of basal surface. Therefore, the epithelial sheets hollowed and concaved structure. It is also reported that mesenchymal cells in ECM secret proteinase and remodel the ECM in intestinal villus morphogenesis[2].

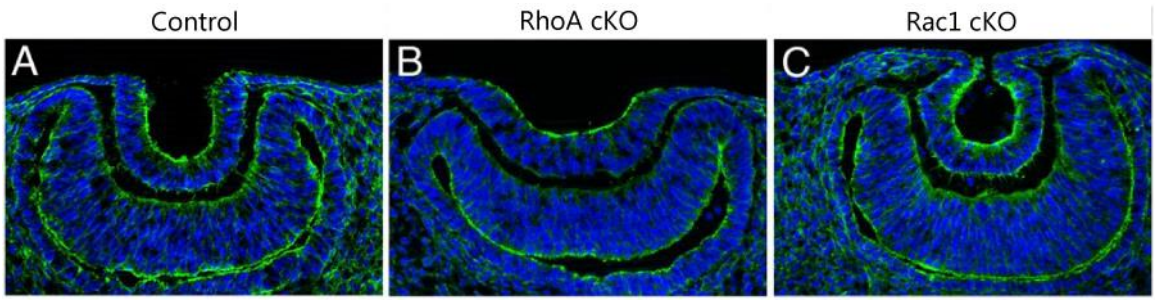

Figure 1-1

Lens placode invagination regulated by RhoA and Rac1 activity[1]

(A) Control, (B) lens pit locally knocked down RhoA (conditional knock out; cKO), (C) Rac1 cKO.

1.2 Extracellular matrix

Cells adhere to extracellular matrix (ECM) that affects cell motility, morphology, and proliferation. ECM consists of basal lamina and connective tissue. Components of basal lamina are largely laminin, type IV collagen, nidogen, and perlecan. On the other hand, that of connective tissue is mainly type I collagen.

1.2.1 Mechanical property of ECM

ECM has mechanical and chemical property. Mechanical property of ECM is stiffness, flexibility, and geometrical constraints. Chemical property of ECM is components such as proteins and soluble factors which ECM contains. In this study, we focused on the relationship between mechanical property of ECM and 3D morphogenesis of epithelial cells. We mention about structure of cross-linked laminin and collagen, main components of ECM. The structure of these proteins determines the mechanical property of ECM.

Laminin

Laminin is main components of basal lamina and is trimeric protein composed of α, β, γ

chain. It is reported that there are 5 types of α chain, 3 types of β chain and 3 types of γ chain and there are many laminin isoforms by combination of αβγ chain[3] (Table 1-1). The structure of laminins is like a cross (Figure 1-2). Laminins can bind to various proteins such as integrin, perlecan, and nidogen. It is known that laminin is necessary to form various tissues, and inhibition of laminin function affect the formation of salivary glands, alveoli, and mammary glands[4].

Collagen

In multicellular organism, collagen is mainly contained in ECM, and accounts for 30 % of the amount of total protein. Collagen molecule is composed of twisted 3 polypeptides. The polypeptide is formed from repetitive structure (Gly-X-Y) (Figure 1-3).

Collagen forms 2 types of structure, fibrous and mesh. Fibrous collagen such as type I collagen forms gel under the condition of 0.14 M salt concentration, pH 7.4, and 37°C, whereas mesh collagen such as type IV collagen forms mesh structure. These collagens have roles in reduction of extracellular stress and regulation of cell adhesion and motility[5].

Laminin-1: $\alpha 1\beta 1\gamma 1$
Laminin-2: $\alpha 2\beta 1\gamma 1$
Laminin-3: $\alpha 1\beta 2\gamma 1$
Laminin-4: $\alpha 2\beta 2\gamma 1$
Laminin-5: $\alpha 3A\beta 3\gamma 2$
Laminin-5B: $\alpha 3B\beta 3\gamma 2$
Laminin-6: $\alpha 3\beta 1\gamma 1$
Laminin-7: $\alpha 3\beta 2\gamma 1$
Laminin-8: $\alpha 4\beta 1\gamma 1$
Laminin-9: $\alpha 4\beta 2\gamma 1$
Laminin-10: $\alpha 5\beta 1\gamma 1$
Laminin-11: $\alpha 5\beta 2\gamma 1$
Laminin-12: $\alpha 2\beta 1\gamma 3$
Laminin-14: $\alpha 4\beta 2\gamma 3$
Laminin-15: $\alpha 5\beta 2\gamma 3$

Table 1-1

Laminin isoforms[3]

It has been reported that 15 isoforms are exist by combination of αβγ chain.

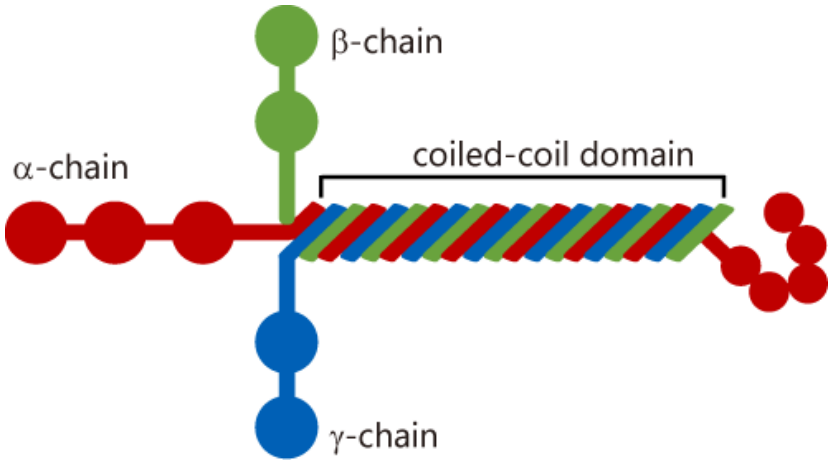

Figure 1-2

Cross link-like structure of laminin

Laminin is trimetric protein. αβγ chains form coiled-coil domain and three branches. Each N-terminal binds to various proteins.

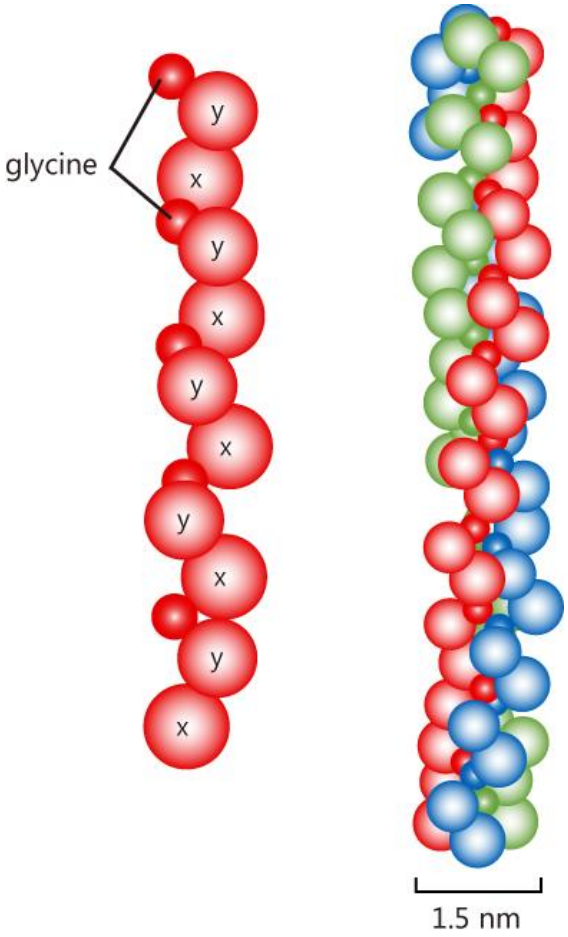

Figure 1-3

Structure of collagen peptide and molecule

(left) Collagen polypeptide has repeated structure. (right) Collagen molecule is composed of twisted 3 polypeptides.

1.3 Multicellular morphology regulated by mechanical property of ECM

Epithelial cells composing tissues receive mechanical stimuli from the ECM. Mechanical properties of the ECM such as stiffness, flexibility, and geometrical constraints are understood as factors that affect the cell behavior[6-13]. For instance, when focusing on substrate stiffness, MDCK cells migrate collectively toward one direction when cultured on a soft collagen gel[8]. It is also reported that the elasticity of the basement membrane is necessary to form the structures that accompany tissue compartmentalization in the zebrafish development[14]. A recent study reveals that epithelial cell directional motility is improved when the contribution of the substrate viscosity is larger than that of its elasticity[11]. Furthermore, in computer simulations, 3D morphological change is induced by the substrate viscosity around cell masses[15].

1.4 Cellular traction forces

During cell movement, division, and maintenance of cell shape, cells regulate their size and shape by exerting cellular traction forces. Cellular traction forces are generated by stress fiber composed of actin filament and myosin II.

1.4.1 Stress fiber

Stress fiber is fibrous structure which mainly comprises actin filament and myosin II (Figure 1-4). Actin filaments linked by α-actinin bind to myosin II bundle. Stress fibers, part of cytoskeleton, have a key role as contractile apparatus. Cellular traction forces generate by sliding of actin and myosin II filament.

1.4.2 Interaction of actin and myosin

As mentioned above, actin and myosin II filament interact and generate traction forces. Sliding motion of actin and myosin II filaments are induced by ATP binding and hydrolysis as described below.

1) ATP binds to myosin head, then the myosin induces conformation change and dissociate from the actin filaments (Figure 1-5A).

2) ATP binding to the myosin is hydrolysed. Subsequently, myosin head alters conformation and move along the actin filaments. ATP is hydrolysed into ADP and inorganic phosphate (Figure 1-5B, Pi). ADP and Pi remain bound to myosin head (Figure 1-5B).

3) After releasing ADP and Pi, myosin binds to actin filaments again (Figure 1-5C and D).

4) By repeating the step 1-3, stress fibers contract.

1.4.3 Cellular traction forces regulated by phosphorylated MRLC

It is crucial that myosin II regulatory light chain (MRLC) phosphorylates for the interaction of actomyosin. Myosin II is composed of myosin heavy chain (MHC), MRLC, and myosin essential light chain (MELC) (Figure 1-6). MRLC has a role in regulation of the actin-myosin interaction. The phosphorylation of MRLC activates the binding site of myosin II and actin filament. As a result, myosin bundles are formed and integrated into stress fibers.

The traction forces of stress fiber are also regulated by MRLC phosphorylation. Previously, our group reported the close relationship between the MRLC phosphorylation

and the traction forces induced by stress fiber[16]. There are two phosphorylation sites in MRLC, threonine 18 and serine 19. Serine 19 is phosphorylated prior to threonine 18[17]. It is well-known that di-phosphorylation of MRLC enhances the degree of elasticity and the traction force of a single cell[16]. Therefore, the spatial distribution of the cellular traction forces is represented by phosphorylated-MRLC localization in the cells. Figure 1-7 shows the relationship between MRLC phosphorylation and cellular traction forces.

The signaling pathways involved in MRLC phosphorylation have been previously described. For instance, the small G protein, RhoA, activates the Rho-associated coiled-coil forming protein kinase (Rho-kinase), which then phosphorylates MRLC[18]. Alternatively, myosin II light chain kinase (MLCK) is also known as an MRLC kinase, which is regulated by calcium and calmodulin[19,20].

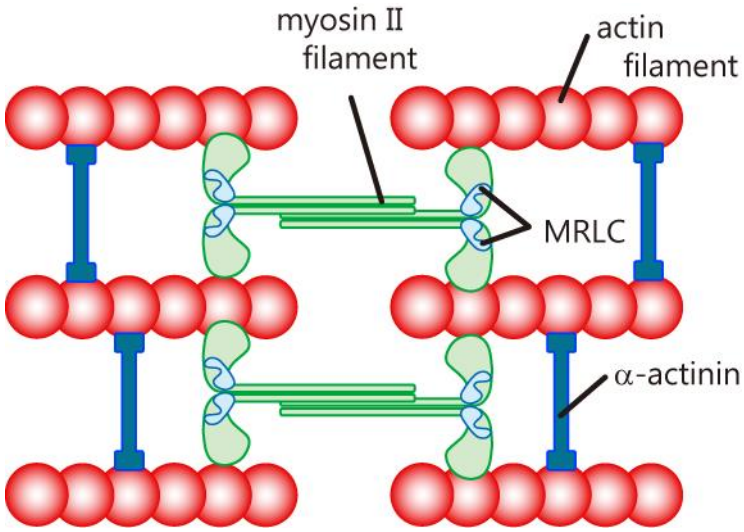

Figure 1-4

Structure of stress fiber

Myosin II filament (green) and actin filament (red) interact each other. Myosin II head binds to actin filament. Actin filaments are linked by α-actinin (blue).

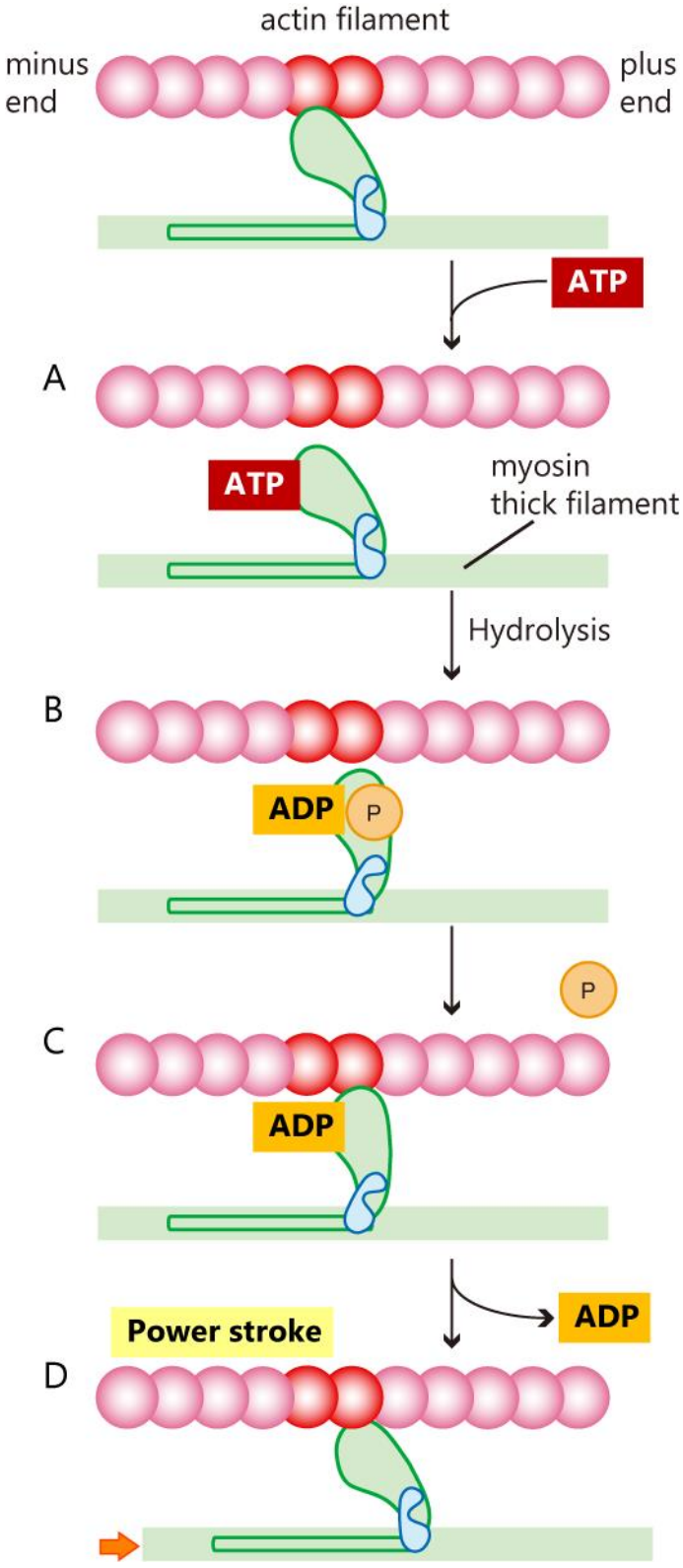
actin filament
minus end
plus end
ATP
A
ATP
myosin thick filament
Hydrolysis
B
ADP
P
P
C
ADP
ADP
Power stroke
D

Figure 1-5

Actin and myosin generate traction force.

(A) Dissociation of myosin head from actin filament by binding ATP. (B) Conformation change of myosin. ATP is hydrolysed to ADP and inorganic phosphate (Pi). (C and D) myosin head binds again to actin filament after releasing ADP and Pi.

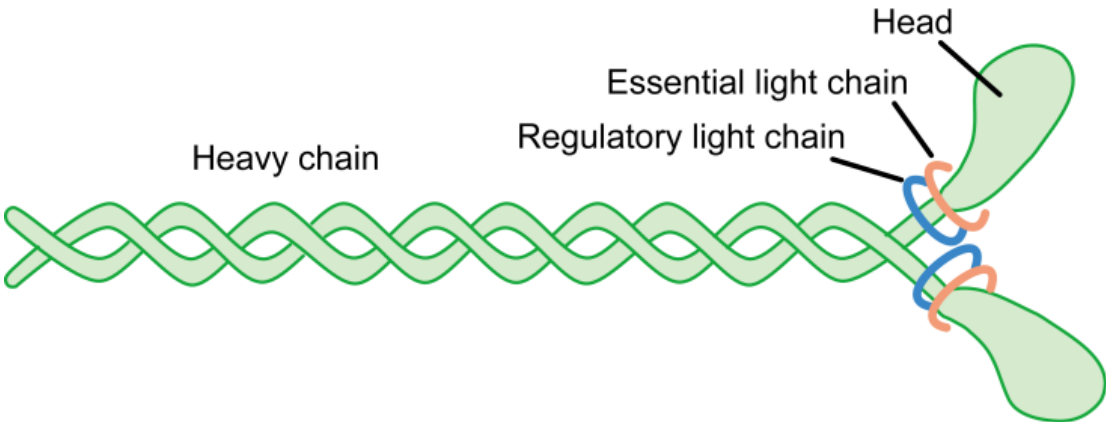

Figure 1-6

Structure of myosin II

Myosin II is composed of myosin heavy chain (MHC), MRLC, and myosin essential light chain (MELC). There are head (right side) and tail (left side) parts of MHC.

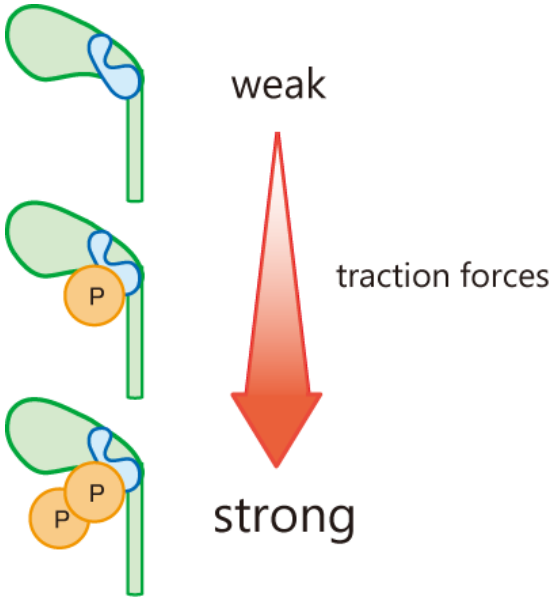

Figure 1-7

The relationship between phosphorylation of MRLC and intensity of traction force.

1.5 Multicellular morphogenesis is regulated by cellular traction forces

Multicellular morphology is regulated by cellular traction forces of stress fibres, which consist of actin and myosin II filaments[21-28]. The relationship between morphogenesis and cellular traction forces was recently investigated *in vivo* and *in vitro*. During tissue invagination and furrow formation during the development process, cellular traction forces support the proper morphogenesis. In the development of a mouse lens, the balanced activities of small G proteins, Rac1 and RhoA, were shown to control cell shape and support proper lens morphogenesis[1]. Moreover, the inhibition of RhoA, Rho-kinase, and myosin II activities in MDCK cells led to the inversion of the orientation of epithelial cell polarity, resulting in abnormal cyst formation[22]. Despite the fact that epithelial cells are well known to present various morphologies, the mechanism underlying morphogenesis remains unclear.

1.6 Purpose of this study

The relationship between living cell 3D morphogenesis and the substrate viscosity has not been clarified. In this study, we tried to observe morphologies of epithelial cells on a viscous substrate. Furthermore, we investigated the relationship between 3D morphogenesis and cellular traction force.

Chapter 2

Materials and Methods

2.1 Preparation of viscous substrata

We used matrigel as the extracellular matrix. Matrigel was extracted from Engelbreth-Holm-Swarm (EHS) mouse sarcoma, a tumour rich in extracellular matrix proteins, and stored at –20°C. The matrigel was thawed overnight at 4°C before use. In this study, we prepared two matrigel substrates, non-treated matrigel (NT-Matrigel) and genipin (Wako Pure Chemical Industries, Ltd., Osaka, Japan) -treated matrigel (GP-Matrigel). In NT-Matrigel, liquefied matrigel was poured into a sample dish and incubated for 30 min at 37°C for solidification. The method used for GP-Matrigel is described in the Chapter 3.

2.2 Cell Culture

MDCK cells were obtained from the Riken Cell Bank and were cultured in Dulbecco's Modified Eagle's Medium (DMEM; Sigma, St. Louis, MO, USA) containing 10% bovine foetal serum (FBS; Equitech Bio Inc., Kerrville, TX, USA), and 1% antibiotic (Invitrogen, Carlsbad, CA, USA). Cells were incubated at 37°C in a humidified incubator with 5% CO_2. The trypsinized cell suspension was plated onto the substrate surface. After incubating for 4 days, the dishes were used for biological experiments.

2.3 Inhibitors

We used Blebbistatin (Enzo Life Sciences, Farmingdale, NY, USA) to inhibit non-muscle myosin II, Y-27632 (Sigma, St. Louis, MO, USA) to inhibit Rho-kinase activity, and ML-7 (Sigma) to inhibit MLCK. Inhibitors were diluted in DMSO (Wako Pure Chemical Industries, Ltd.) except for Y-27632. We prepared a DMSO-treated sample as a control. The cells were treated with the following concentrations for 24 h or 4 days, 10 μM Blebbistatin, 10 μM Y-27632, and 2 μM ML-7.

2.4 Time-lapse observations

The sample dishes were filled with culture medium and sealed with silicone grease to avoid changes in the medium pH. Time-lapse observations were conducted with a phase-contrast microscope (TE2000; Nikon, Tokyo, Japan) equipped with a 10× objective, which was kept in an acrylic resin box to maintain the temperature at 37°C. Time-lapse images were captured every 5 min with Image-pro software (Media cybernetics Inc., Silver Spring, MD, USA). In matrigel deformation analysis, latex beads (2 μm; Polysciences, Inc., Warrington, PA, USA) were embedded in the matrigel to observe any deformations induced by the cellular traction forces.

2.5 Immunofluorescence

Cells were fixed with 1% or 2% formaldehyde in phosphate-buffered saline (PBS) for 5 min, permeabilized with 0.5% Triton-X100 in PBS for 5 min, and blocked with 0.5% bovine serum albumin (Sigma) or 0.5% skim milk (Megmilk Snow Brand Co., Ltd., Sapporo, Japan) in PBS. Reaction with the primary antibody was performed at room temperature overnight. The primary antibodies used were L9393 (Sigma) for laminin-111, anti-phospho-MRLC (Ser 19) mouse IgG (Cell Signaling Technology Japan, K.K., Japan), and anti-phospho-MRLC (Thr18/Ser19) rabbit IgG (Cell Signaling Technology) at a dilution of 1:250, 1:200, and 1:200, respectively. All samples were incubated with a mixed solution consisting of the secondary antibody and Alexa Fluor-488 phalloidin (Invitrogen) for F-actin staining at 37°C for 1 h. AlexaFluor-594 goat anti-rabbit IgG (H+L) and AlexaFluor-546 goat anti-mouse IgG (H+L) were used as secondary antibodies (Molecular Probes, Eugene, OR, USA) at a concentration of 10 μg/mL. Fluorescent images were captured using confocal laser scanning microscopy (C1 confocal imaging system; Nikon). We used the Imaris software (Bitplane AG, Zürich, Switzerland) for 3D reconstruction of confocal images. This software enabled the visualization of 3D morphologies of the epithelial cells.

The anti-laminin-β1 mouse IgG (2E8), anti-integrin-β1 (AIIB2) from Developmental Studies Hybridoma Bank (University of Iowa, Iowa City, IA, USA), and anti-gp135 mouse IgG (3F2; kindly provided by Prof. Ojakian) were used as primary antibodies at a dilution of 1:200, 1:200, and 1:300, respectively. Reaction with the primary antibody was performed at room temperature overnight. The secondary antibody and Alexa Fluor-488 phalloidin for F-actin staining were used as described in the Materials and Methods section.

2.6 Western blotting

We extracted proteins from the cells plated on matrigel-coated dishes. For fixation, the culture medium was removed from the dish and ice-cold 10% trichloroacetic acid (Sigma) in PBS was added. After washing with PBS, 200 μL SDS sample buffer (0.25 M Tris–HCl pH 8.8, 5% dithiothreitol, 2.3% sodium dodecyl sulphate, 10% glycerol, and 0.01% bromophenol blue) was added and the cells were lysed. Lysed cells were sonicated and heated at 95°C for 5 min, and stored at – 20°C. We used 12.5% polyacrylamide gels for SDS-PAGE for 75 min and the proteins were transferred onto a polyvinylidene difluoride membrane (Millipore, Bedford, MA, USA). The membrane was blocked with 5% skim milk in TBST solution (10 mM Tris–HCl containing 150 mM NaCl and 0.05% Tween 20, pH 7.5). The primary

antibodies used were anti-phospho-MRLC (Ser 19 or Thr18/Ser19; Cell Signaling Technology) rabbit IgG at 4°C overnight. After three washes with TBST, HRP-conjugated anti-rabbit IgG antibody to reveal phosphorylated-MRLC and HRP-conjugated anti-mouse IgG antibody to reveal GAPDH were used as secondary antibodies at room temperature for 1 h. All antibodies were diluted in Can Get Signal Immunoreaction Enhancer (Solutions 1 and 2; Toyobo, Osaka, Japan). The target protein signal intensity was detected by using Immobilon Western Chemiluminescent HRP substrate (Millipore). GAPDH was used as an internal control, and its expression levels were measured. Image J software (National Institutes of Health, Bethesda, MD, USA) was used to quantify the signal intensity (Figure 3-5D).

2.7 Statistical analysis

Each experiment was repeated at least three times. The error bars represent the mean ± s.e.m. For viscoelasticity measurements and western blotting analysis, open source Image J (National Institutes of Health) with some plugins was used (Figure 3-1B, D, and 3-5D). Displacement of latex beads embedded in the matrigel was analyzed by using Imaris software (Bitplane AG) (Figure 3-3A and Supplementary Figure 2A), and was described by

box-plot using R software (R Development Core Team, Vienna, Austria) (Figure 3-3B and Supplementary Figure 2B). We performed all statistical analyses using Student's *t*-test, and considered a P-value of <0.05 as significant.

Chapter 3

Results

3.1 Viscosity of matrigel substrate

To modify the matrigel substrate viscosity, we used genipin (GP), a cross-linker of amino group[29-32]. We assumed that increasing cross-links by GP would increase the matrigel viscosity. The GP solution was mixed with the matrigel before solidification at the following concentrations, 0, 0.25, and 0.50 mM (referred to as non-treated (NT)-Matrigel, 0.25-GP-Matrigel, and 0.50-GP-Matrigel, respectively).

To measure the viscosity of the matrigel substrata, we performed an experiment in which a stainless ball was dropped into the matrigel. This experiment is referred to as the ball dropping method hereafter. To observe the stainless ball in the matrigel, we built a thin cylinder by assembling a plastic tube and a cover glass (Figure 3-1A). The radius of the cylinder is 1.5 mm, and its length is approximately 50 mm. GP-Matrigel substrata in the cylinders were incubated at 37°C overnight to solidify and for the cross-linking to occur. After incubation, a stainless ball was set on the gel upper surface. The cylinders were subsequently filled with medium and sealed with oil clay (Figure 3-1A). The sample cylinders were kept in a styrofoam box to maintain the temperature at 37°C. We obtained time-lapse images captured with a camera every 10 min for 48 h (Figure 3-1B and Movie S1). We estimated fall velocities (v) from a linear approximate equation of the displacement-time graph (Figure 3-1C) and calculated viscous moduli (η) using the following equation:

$$\eta = \frac{2}{9} \cdot \frac{r^2(\rho_2 - \rho_1)g}{v},$$

where r is radius of the stainless ball, ρ_1 and ρ_2 represent the density of the matrigel and the stainless ball, respectively, and g is the acceleration of gravity, and their values are as follows: r = 0.75 × 10^{-3} m, ρ_1 = 1.1 × 10^3 kg/m^3, ρ_2 = 0.79 × 10^3 kg/m^3, and g = 9.8 m/s^2. The viscous moduli and estimated fall velocities are described in Figure 3-1D. The viscous moduli of 0.25-GP-Matrigel and 0.50-GP-Matrigel were 1.18–fold and 1.86–fold higher than that of NT-Matrigel, respectively. These results suggest that the matrigel viscosity increased with increasing concentrations of GP.

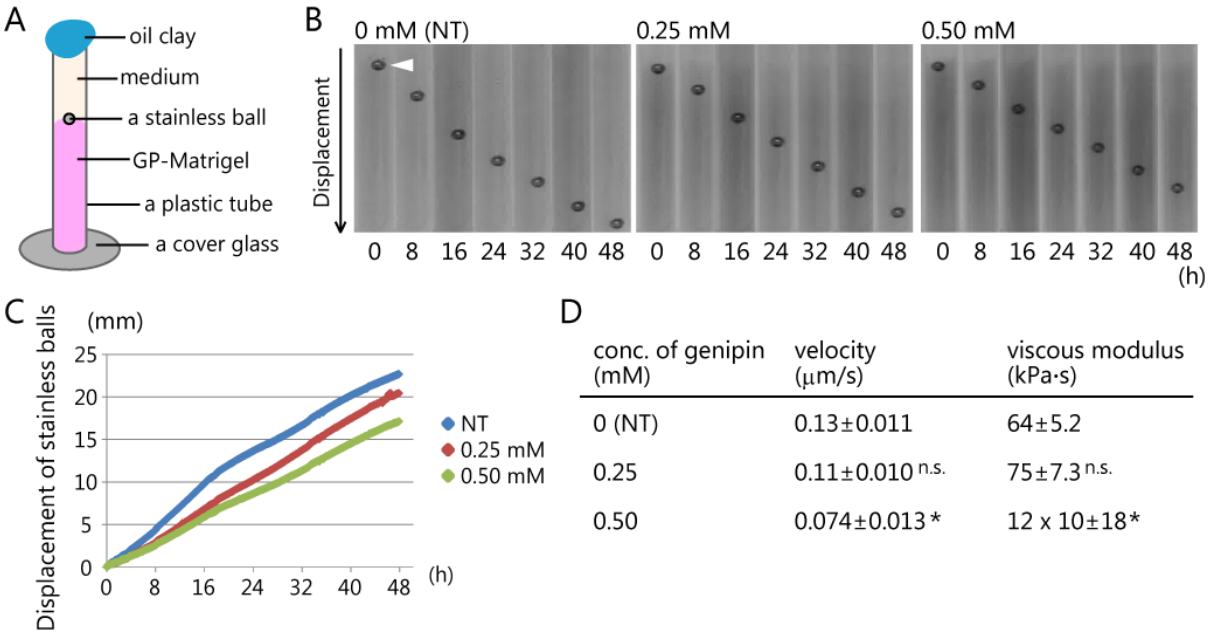

D

conc. of genipin (mM)	velocity (μm/s)	viscous modulus (kPa·s)
0 (NT)	0.13±0.011	64±5.2
0.25	0.11±0.010 n.s.	75±7.3 n.s.
0.50	0.074±0.013 *	12 x 10±18*

Figure 3-1

Measurement of the matrigel viscosity after genipin treatment

(A) Schematic representation of matrigel viscosity measurement conditions. The matrigel used for the measurement was poured into a cylinder built from a plastic tube and a cover glass prior to solidification. After solidification, the gel surface was filled with medium. The radius of the cylinder is 1.5 mm, and its length is approximately 50 mm. The radius of the stainless ball is 0.75×10^{-3} m. The cylinders were sealed with oil clay to prevent changes in the medium pH. (B) Kymographs of the stainless balls in the matrigel. The genipin concentrations in the matrigel are indicated above each image: 0 mM (No-treatment; NT), 0.25 mM, and 0.50 mM. Numbers under the images represent the time relative to the start (0

h) and the end (48 h) of the observation. White arrowhead shows the initial position of the stainless ball. (C) Time-displacement plot of stainless balls through the matrigel. The displacement in the plot corresponds to the result obtained from the time-lapse observations in Figure 3-1B. The horizontal axis is the relative time and the vertical axis is the relative displacement of stainless balls. (D) Mean velocities of stainless balls and the matrigel viscous moduli. The mean velocities are the gradients of the linear approximate equations. This experiment was repeated three times. Each value represents the mean value ± standard error of the mean (s.e.m.). Statistical significance between NT and other two samples: n.s., $p \geq 0.05$, *, $p < 0.05$.

3.2 3D morphology of MDCK cells on the matrigel substrate

To observe MDCK cell morphologies on the NT-Matrigel substrate, we cultured the cells for 4 days and performed immunofluorescence staining for F-actin and laminin-111. Laminin-111 is a major component of the matrigel. Thus, we can identify the substrate surface. The F-actin staining indicated that MDCK cells formed a 3D structure resembling a tulip hat on the NT-Matrigel (Figure 3-2A and 3-2D). Moreover, laminin-111 staining showed that the inside of the tulip hat was filled with the matrigel substrate (Figure 3-2A). This result indicates that the MDCK cells grown on the NT-Matrigel deformed the substrate and formed a 3D tulip hat-like morphology.

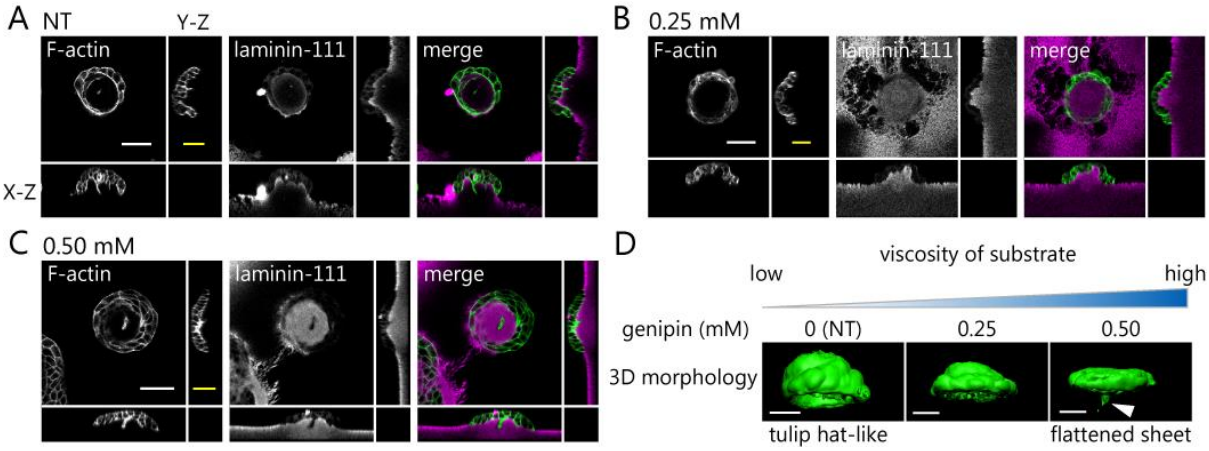

Figure 3-2

MDCK cell morphological change on genipin-treated matrigel

(A-C) Immunofluorescence images of MDCK cells on genipin-treated matrigel. The concentrations of genipin are (A) 0 mM (NT), (B) 0.25 mM, and (C) 0.5 mM. The cells and matrigel surface structure are detected by F-actin and laminin-111 staining, respectively. Cross-sectional views are shown together. Scale bar (white) = 50 μm. Scale bar (yellow) = 20 μm. (D) Relationship between cell morphology and substrate viscosity. The images of 3D morphology were reconstructed using the results presented in a-c. White arrowhead shows the protrusion-like structure in the 3D structure. Scale bar = 30μm.

3.3 MDCK cell 3D morphological changes depending on the matrigel viscosity

To investigate the relationship between cell morphology and substrate viscosity, MDCK cells were cultured on the different GP-Matrigels for 4 days. F-actin and laminin-111 staining indicated that MDCK cells on 0.25-GP-Matrigel formed a 3D structure similar to that of the cells cultured on NT-Matrigel. However, the height of the structure above the matrigel surface was lower compared with that the structure obtained on NT-Matrigel (Figure 3-2D). In 0.50-GP-Matrigel, MDCK cells did not present a 3D tulip hat-like morphology, but formed a monolayer sheet (Figure 3-2C and 3-2D). Additionally, a protrusion was found beneath the monolayer sheet (Figure 3-2D, white arrowhead). While we previously reported the existence of a protrusion with cells cultured on matrigel within 2 days[33], the reason why the protrusion appeared remains unclear. The relationship between cell morphology and the substrate viscosity is shown in Figure 3-2D. These results imply that MDCK cell morphology varied according to the substrate viscosity.

3.4 Substrate deformation induced by cellular traction force

The staining of the matrigel surface revealed that the pericellular substrate was deformed. To observe the deformation of the matrigel surface during 3D morphogenesis, we embedded latex beads in the matrigel and followed the bead movement and the matrigel deformation. Time-lapse observations for 24 h showed that the latex beads moved toward the cell masses. Green lines in Figure 3-3A and Movie S2 exhibit the beads trajectories that occurred within 1.5 h. This result indicates that MDCK cells exerted forces on the matrigel and deformed the peripheral substrate. Thus, we postulated that the matrigel deformation resulted from the cellular traction forces. We then blocked the cellular traction forces by treatment with inhibitors and conducted time-lapse observations. We treated the cells with a Rho-kinase inhibitor (Y-27632; 10 μM). Y-27632 promotes the dephosphorylation of MRLC[34]. Time-lapse observation showed that the displacement of latex beads was halted (Figure 3-3A and Movie S3). The median value of displacement velocity was about 10 times slower than that in NT conditions (Figure 3-3B, ****, $p < 0.0001$). These results suggest that the cellular traction forces induced by MRLC phosphorylation are involved in the matrigel deformation.

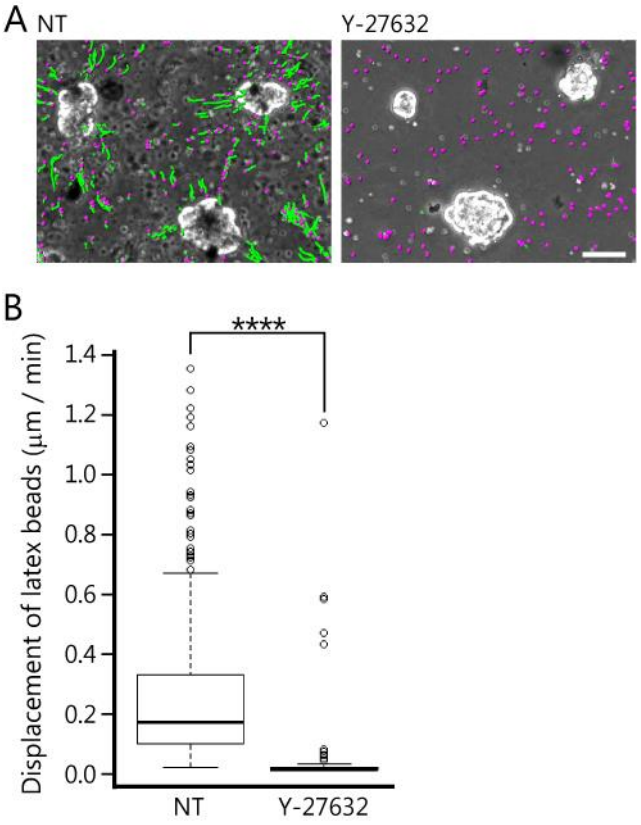

Figure 3-3

The matrigel surface is deformed during the 3D morphogenesis

(A) Trajectories of latex beads embedded in the matrigel. The beads are shown as magenta spheres and the trajectories of the beads are shown as green lines. The green lines represent the displacement for 1.5 h. NT: No reagent control, Y-27632: Rho-myoikinase inhibitor (10 μM). For this analysis, more than 50 latex beads were randomly chosen from each condition. Scale bar = 50 μm. (B) The box plot shows the displacement of embedded latex beads. Error bars represent s.e.m. ****, $p < 0.0001$.

3.5 The cellular traction forces involved in 3D morphogenesis on matrigel

To examine whether cell morphology varies by blocking the cellular traction forces, we observed cell morphology on the matrigel in the presence of inhibitors. The cells were treated with inhibitors of myosin II activity (Blebbistatin; 10 μM), Rho-kinase (Y-27632; 10 μM), and MLCK (ML-7; 2 μM) continuously for 3 days. The substrate deformation was blocked by treatment with blebbistatin and Y-27632, but not by ML-7 treatment (Figure 3-4C-E). Furthermore, to compare the difference in cell morphology among the samples, we chose 30 colonies at random from one sample and categorized cell morphologies into three types, a tulip hat-like structure, a flattened sheet, and others. This analysis was repeated three times. The percentage of each structure is represented in Figure 3-4F. Tulip hat-like structures accounted for 70–80% of the total cell morphology under NT and dimethyl sulfoxide (DMSO) conditions. In contrast, treatment with blebbistatin and Y-27632 caused a dramatic reduction of the number of tulip hat-like structures (****, $p < 0.0001$, and ***, $p < 0.001$) and increased the number of monolayer sheet structures. In ML-7 treatment conditions, the tulip hat-like structures accounted for approximately 60% of the total cell morphology, although there was a significant reduction in the number of tulip hat-like structure in comparison to NT conditions (*, $p < 0.05$). Additionally, flattened sheet

structures were not observed at all. These results imply that myosin II activation and MRLC phosphorylation by Rho-kinase are involved in the morphological changes observed on matrigel.

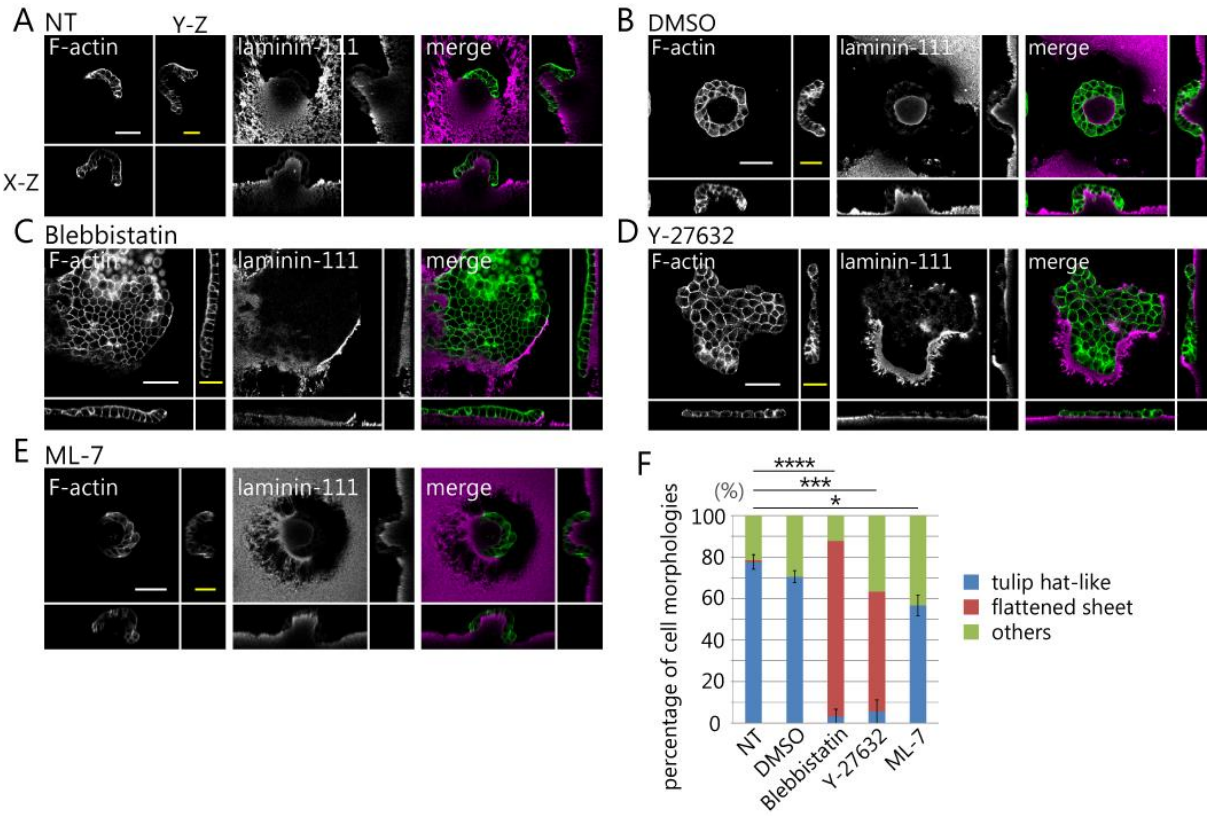

Figure 3-4

Morphological change of MDCK cells treated with inhibitors

(A-E) Immunofluorescence staining of the cells and matrigel surface. The conditions are the following: (A) No-treatment (NT), (B) DMSO as a control for the following reagents except for Y-27632, (C) Blebbistatin, (D) Y-27632, and (E) ML-7. Orthogonal views are shown together. Scale bar (white) = 50 μm. Scale bar (yellow) = 20 μm. Three colonies were randomly chosen in each experiment (N = 3 (at least)). (F) The graph indicates the proportion of cell structures. Cell structures are categorized into three morphology types: tulip hat-like structure, monolayer sheet, and others. Thirty colonies were randomly chosen

in three independent experiments (N = 3). Results are shown as mean value ± s.e.m. *, $p < 0.05$, ***, $p < 0.001$, ****, $p < 0.0001$

3.6 Spatial distribution of phosphorylated MRLCs in the 3D tulip hat-like structure

To determine the area where the cellular traction forces were exerted within the 3D structure, the cells were immunostained for phosphorylated MRLC (P-MRLC). P-MRLC localization represents the spatial distribution of the cellular traction force. Immunofluorescence imaging was performed to observe P-MRLC in MDCK cell 3D morphology. MRLC has two phosphorylation sites, threonine 18 and serine 19. MRLC di-phosphorylation enhances the degree of elasticity and the traction force[9,16]. In NT and DMSO treated samples, we found that mono- and di-phosphorylated MRLC (1P-MRLC and 2P-MRLC) localized along the periphery of the tulip hat-like structure (Figure 3-5A and B, arrowheads). 1P-MRLC and 2P-MRLC localization toward the outer edge of the epithelial sheet structure disappeared when the cells were treated with 10 μM Y-27632 (Figure 3-5C). In addition, MDCK cells formed a flattened sheet. On the other hand, the cells formed a 3D tulip hat-like structure and the localization of both 1P- and 2P-MRLC was preserved when the cells were treated with ML-7 (Figure 3-5D, arrowheads). Furthermore, we detected 1P-MRLC and 2P-MRLC phosphorylation in cells treated with Y-27632 and ML-7 by western blotting. Both 1P-MRLC and 2P-MRLC significantly decreased after treatment with 10 μM Y-27632 (**, $p < 0.01$), and 1P-MRLC decreased after treatment with 2 μM ML-7 (*, $p < 0.05$, Figure 3-5E and F). These

results indicate that 2P-MRLC localization toward the outer edge of the epithelial sheet is essential for the 3D tulip hat-like morphogenesis, though MRLC mono-phosphorylation also affects it.

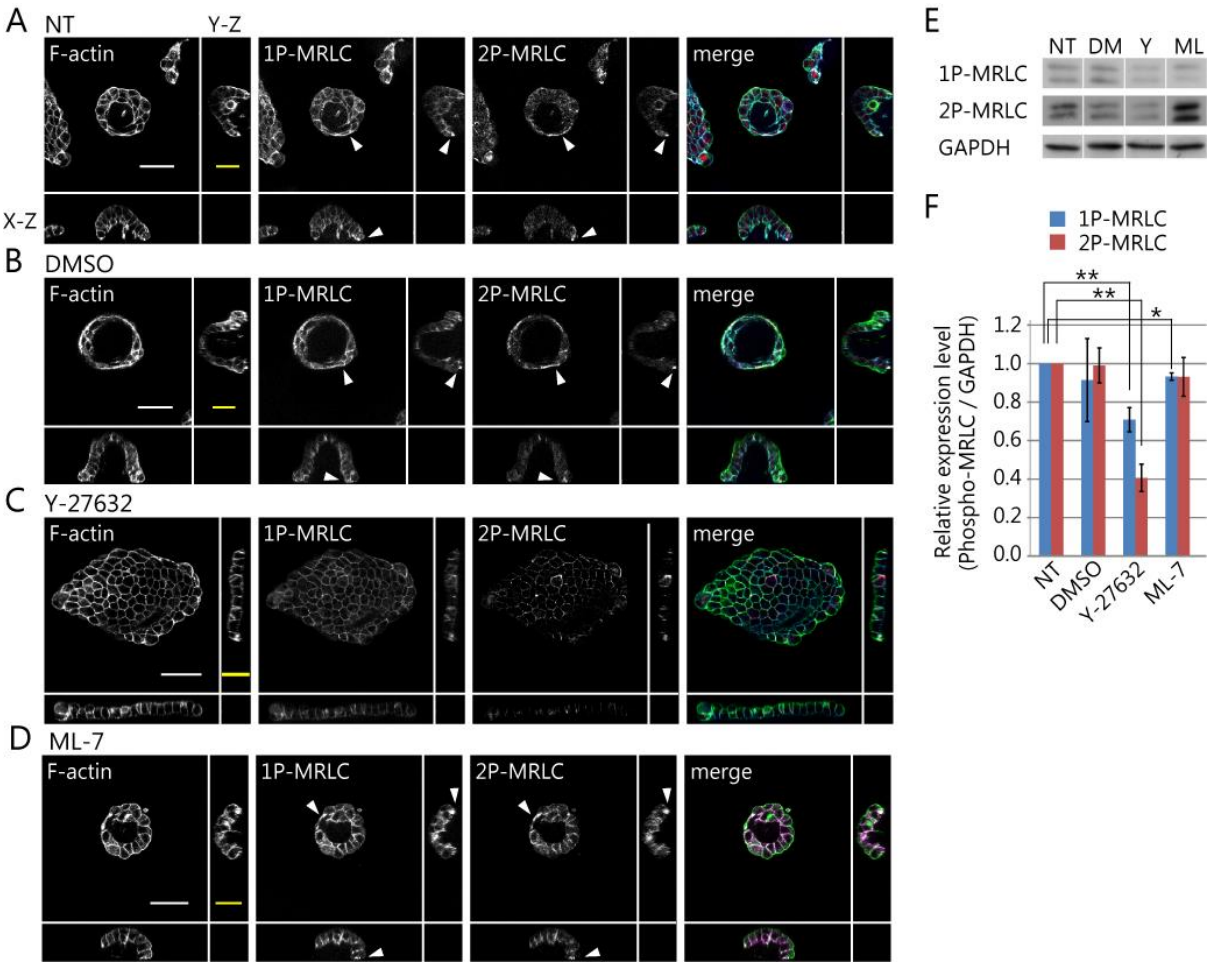

Figure 3-5

Localization and expression of phosphorylated-MRLC in the cells

(A-D) F-actin, 1P-MRLC, and 2P-MRLC staining on the matrigel surface. Each sample was treated with (A) no reagent (NT), (B) DMSO as a control, (C) Y-27632, and (D) ML-7. Cross-sectional views, X-Z, and Y-Z plane are shown together. White arrowheads in the images represent 1P-MRLC and 2P-MRLC localization. Three colonies were randomly chosen in each experiment (N = 3 (at least)). Scale bar (white) = 50 μm and scale bar (yellow)

= 20μm. (E and F) Immunoblot and statistical analysis of 1P-MRLC and 2P-MRLC protein expression in MDCK cells cultured on matrigel-coated dishes. The cells cultured on non-treated matrigel were used as control. Mean values are calculated from three independent experiments. Error bars represent s.e.m. *, $p < 0.05$, **, $p < 0.01$.

Chapter 4

Discussion

We suggest a model for epithelial cell 3D morphogenesis on a viscous substrate induced by the cellular traction forces (Supplementary Figure 1). On viscous substrate like matrigel, epithelial cells form a 3D tulip hat-like structure. Moreover, as the substrate viscosity increased, the structure formed by epithelial cells changed to a flattened sheet structure (Supplementary Figure 1A). We also confirmed that deformation of the peripheral substrate decreased with increase in substrate viscosity (Supplementary Figure 2 and Movie S4-6). Concomitantly, the cells exerted traction forces at the edges of the cell sheets (Supplementary Figure 3 and 1A, indicated by red dots). The amount of cross-link formation (Supplementary Figure 1A, blue dots) contributes to substrate viscosity (Supplementary Figure 1A). Supplementary Figure 1B shows the relationship between the multicellular morphology and the cellular traction forces. The epithelial cells generate traction forces at the edge of the cell sheet toward the centre that causes the matrigel deformation, resulting in epithelial cells forming 3D tulip hat-like structures (Supplementary Figure 1B). Collectively, our results suggest that the observed 3D morphogenesis involved three important factors, the substrate viscosity, the substrate deformation, and the cellular traction forces induced by P-MRLC.

Epithelial cells grown on matrigel exerted cellular traction forces on the peripheral substrate and changed the substrate shape (Figure 3-2A and 3-3A). On the other hand, it is known that epithelial cells on a collagen gel do not form 3D tulip hat-like structures and do

not remodel the peripheral substrate[8]. To explain the cell-induced matrigel deformation, we focused on the difference in the protein cross-links formed in these gels. Biomimetic substrates such as matrigel and collagen type I gel are known as physical gels. The molecule bindings in the physical gel are unstable and are repeatedly dissociated and associated by external forces and thermal energy[32,35,36]. The gel physical properties depend on the formation of cross-links between proteins. Laminin and type IV collagen in the matrigel form mesh structures, whereas type I collagen forms fibrous structures[37-40]. The flexibility and fluidity of the substrate are controlled by the amount of cross-linking formation[11,41]. In the present study, the matrigel did not deform when the matrigel viscosity was increased by GP treatment (Figure 3-2). The GP-induced a cross-link, which is a chemical binding that is robust and durable[30-32,42]. This result means that the substrate deformation was blocked because of a decrease in the fluidity induced by GP. Thus, we conclude that the cross-link structure largely affects the matrigel deformability. Consequently, the deformation of the pericellular matrigel by the cellular traction forces is easier than that of the type I collagen gel.

Differences between collagen gel and matrigel are not limited to those of cross-linking formation. In the present study, we use matrigel, a biomimetic material, containing various proteins such as laminin-111, type IV collagen, and soluble growth factors. Collagen gel is a

material composed of type I collagen only. Proteins and growth factors in the gel affect cell behaviour such as migration, morphology, and proliferation[43-45]. Therefore, in the future, we plan to design a viscous substrate that circumvents these issues.

The epithelial cells on the matrigel presented a 3D tulip hat-like morphology (Figure 3-2A). *In vivo*, similar 3D structures are observed during notochord tubulogenesis, brain morphogenesis, and optic cup formation[25,46,47]. The epithelial cell sheets hollow and form convex structures, caused by basal constriction. Networks of actomyosin and microtubule, laminin secretion, and focal adhesion components are the key factors of basal constriction[25,46,47]. These studies showed the importance of cell-substrate adhesion for basal constriction. Integrins localize at the plasma membrane and transduce signals from laminin to actomyosin via focal adhesion. We performed immunostaining for gp135, an apical marker, and laminin-β1, a basal marker. The results showed that the apico-basal polarity in the tulip hat-like structure was maintained (Supplementary Figure 4). Furthermore, we observed the localization of integrin β1 toward the basal surface of the tulip hat-like structure (Supplementary Figure 4). Hence, these results imply that the morphogenesis on matrigel can be induced by basal constriction.

In this study, 2P-MRLC localization toward the outer edge of the epithelial sheets was crucial for the 3D morphogenesis of a tulip hat-like structure. To elucidate whether there is a

correlation between 2P-MRLC localization and 3D morphology, flattened epithelial sheets were cultured on matrigel and treated with Y-27632 as shown in Figure 3-4D. After washing out Y-27632, the cell sheets were cultured for another 48 h. F-actin and 2P-MRLC immunostaining was performed to observe the 3D morphology and the cell force spatial distribution. The cells exerted traction forces toward the edge of epithelial sheets after removing the inhibitor. We observed the sparse localization of 2P-MRLC throughout the epithelial sheets (Supplementary Figure 5). In addition, the cell sheets formed structures, which were similar to villi of the small intestine and the sulcus in the brain (Supplementary Figure 5). These results indicate that the 3D morphology depends on the substrate area on which the cells apply forces. We assume that the villus-like structure was formed due to the deformation generated by the sparse distribution of the cellular traction force.

Recently, cell sheet transplant methods have been established in regenerative medicine[48-50]. Artificial organ formation requires that the cell sheets maintain their structures. To evaluate whether the tulip hat-like morphology is a persistent structure, we cultured MDCK cells on NT-Matrigel for 2 weeks and performed immunofluorescence staining of F-actin and laminin-β1, a basal marker. The results showed that the tulip hat-like morphology and cell polarity were maintained (Supplementary Figure 6). The epithelial cell sheet culture on viscous substrate will be applied to artificial organ formation in the future.

In conclusion, this study showed that 3D morphogenesis is induced by the substrate viscosity and the cellular traction forces. We increased the matrigel viscosity by adding a cross-linking reagent. The 3D morphology on the matrigel changed due to the increment of the substrate viscosity. MDCK epithelial cells formed 3D tulip hat-like structures. Additionally, P-MRLC localization is important for 3D morphogenesis on viscous deformable substrates. Our data indicate that the substrate viscosity and the cellular traction force are involved in morphological changes observed during 3D morphogenesis and believe that these factors will affect 3D morphogenesis *in vivo*.

Supplementary Information

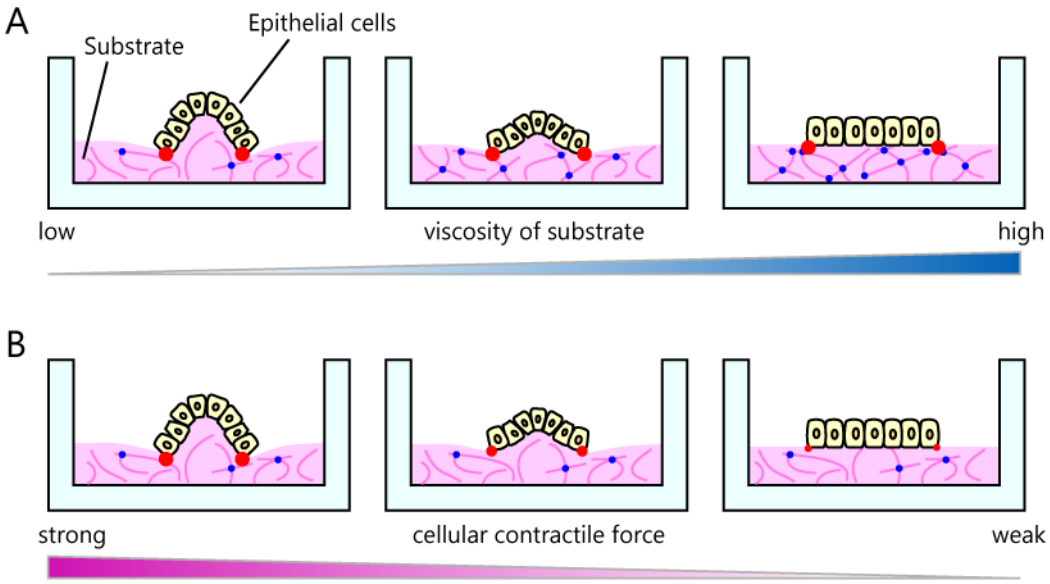

Supplementary Figure 1

A proposed model for epithelial cell 3D morphogenesis induced by the substrate viscosity and cellular traction forces

(A) The morphological change involved the substrate viscosity. The substrate viscosity was altered by the extent of cross-links between peptide chains contained in the matrigel. Pink lines represent the peptide chains. The blue dots represent the cross-linking sites in the peptide chains. Red dots indicate the localization of the cellular traction force and their sizes indicate the strength of the cellular traction force (B) 3D morphology on the viscous substrate changes depending on the strength of the cellular traction force.

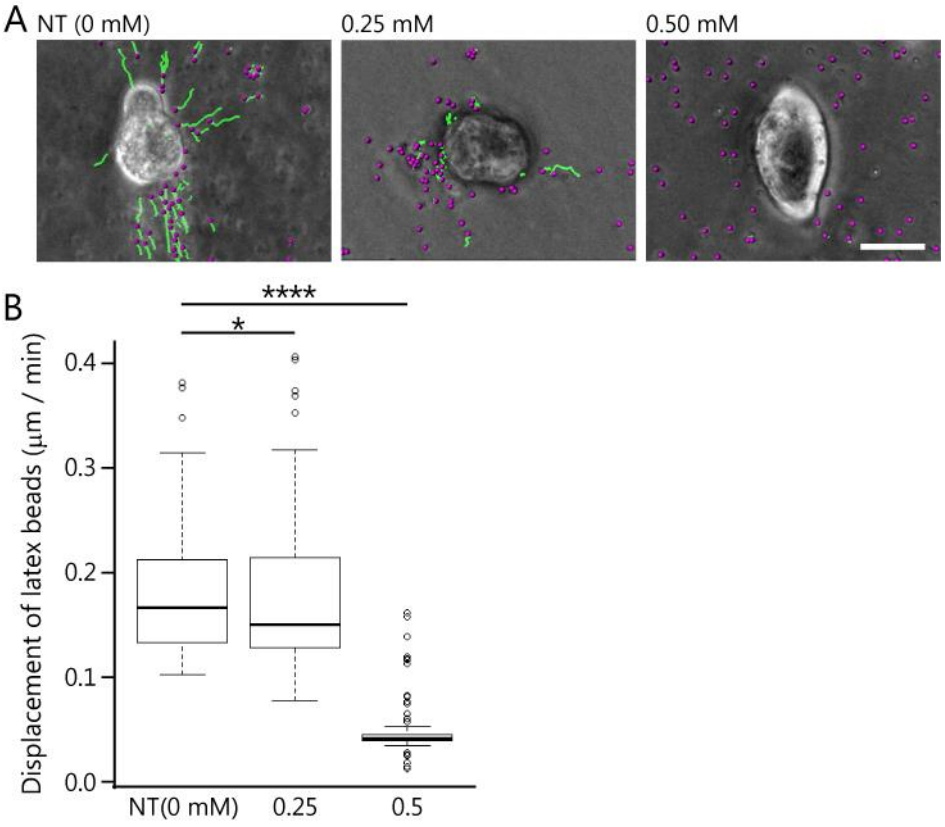

Supplementary Figure 2

The matrigel surface is unchanged with increasing concentration of GP during the 3D morphogenesis on GP-Matrigels

(A) Trajectories of latex beads embedded in the GP-matrigel. The beads are shown as magenta spheres, and their trajectories are shown as green lines. The green lines represent the displacement for 1.5 h. For this analysis, more than 30 latex beads were randomly chosen from each condition. Scale bar = 50 μm. (B) The box plot shows the displacement of embedded latex beads. Error bars represent s.e.m. *, $p < 0.05$, ****, $p < 0.0001$.

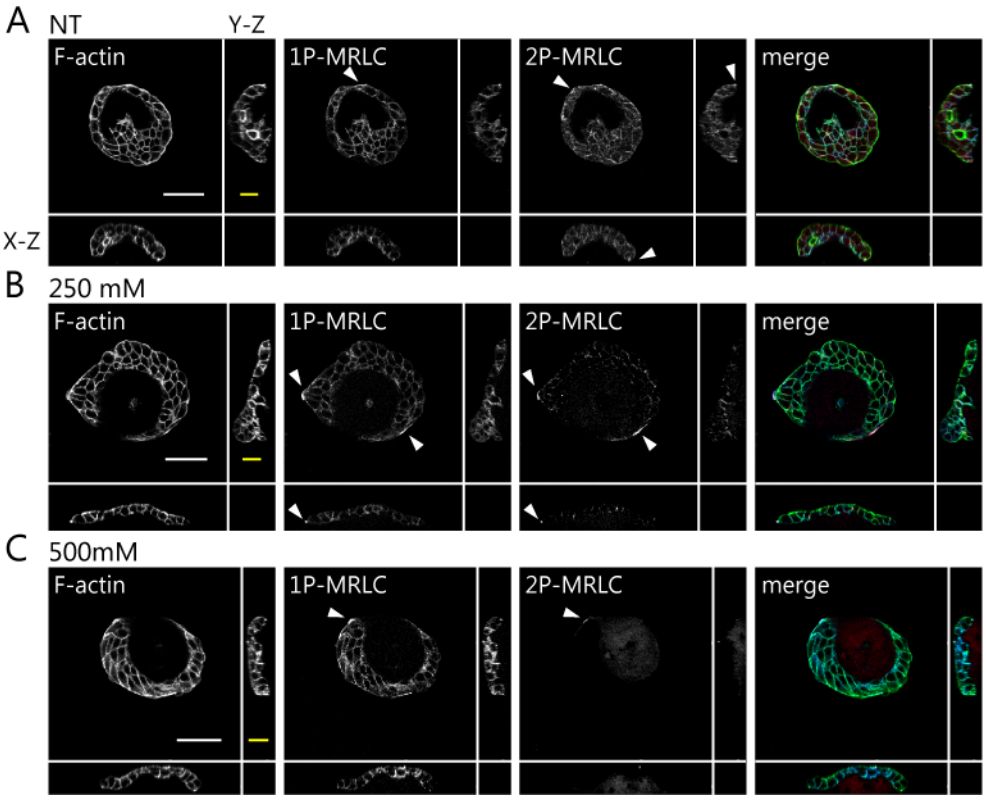

Supplementary Figure 3

Localization of phosphorylated-MRLC in the cells cultured on GP-Matrigel.

F-actin, 1P-MRLC, and 2P-MRLC staining on the matrigel surface. MDCK cells cultured on (A) NT-GP-Matrigel (control), (B) 0.25 mM-GP-Matrigel, and (C) 0.50 mM-GP-Matrigel. Cross-sectional views, X-Z plane and Y-Z plane, are shown together. White arrowheads in the images represent 1P-MRLC and 2P-MRLC localization. Three colonies were randomly chosen in each experiment (N = 3). Scale bar (white) = 50 μm and scale bar (yellow) = 20 μm.

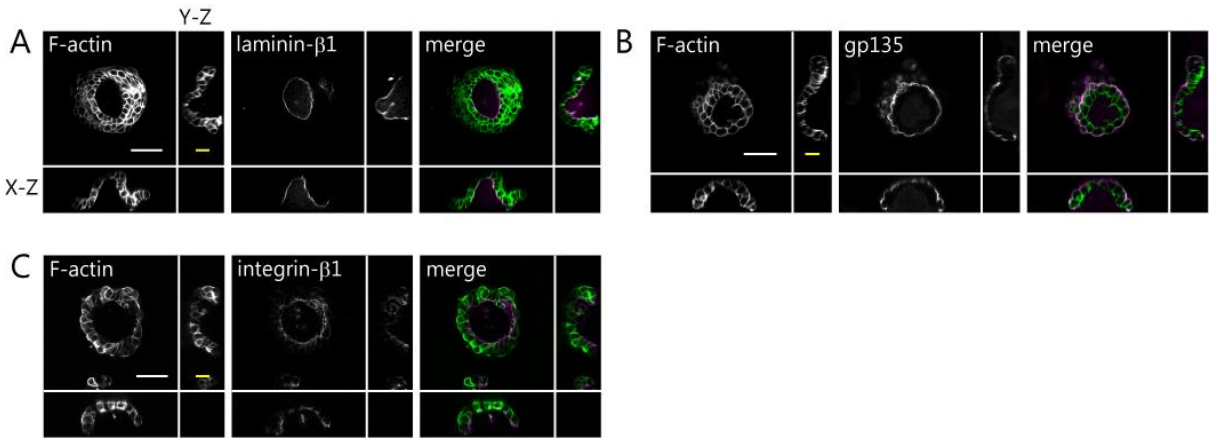

Supplementary Figure 4

Epithelial cell apico-basal polarity is involved in the formation of the tulip hat-like structure. Immunofluorescence images of (A) laminin-β1, (B) gp135, and (C) integrin-β1 in MDCK cells cultured on matrigel. Green: F-actin, magenta: (A) laminin-β1, (B) gp135, and (C) integrin-β1, respectively. Scale bar (white) = 50 μm and scale bar (yellow) = 20 μm.

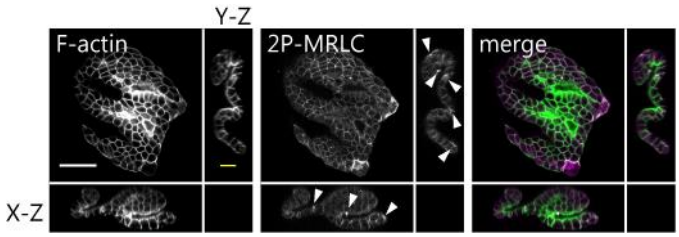

Supplementary Figure 5

3D villi-like structure was observed when the flattened epithelial sheets were cultured on the matrigel for 48 h. Green: F-actin, Magenta: 2P-MRLC. White arrowheads in the figure represent 2P-MRLC localization. Scale bar (white) = 50 μm and scale bar (yellow) = 20 μm.

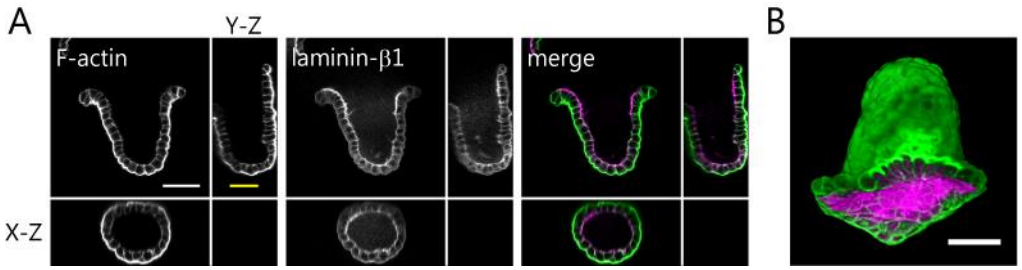

Supplementary Figure 6

The 3D tulip hat-like morphology was maintained for 2weeks.

(A) Immunofluorescence images of the tulip hat-like morphology of cells cultured on NT-Matrigel. Green: F-actin, Magenta: laminin-◎1. Cross-sectional views are shown together. Scale bar = 50 μm. (B) 3D reconstruction image of (A). The image of the 3D tulip hat-like morphology was reconstructed using the results presented in (A). Scale bar (white) = 50 μm and scale bar (yellow) = 20 μm.

Movie S1

Time-lapse movie of a stainless ball dropped into the matrigel. The numbers in the movie represent GP concentrations. In the movie, 1 s = 300 min in real time.

Movie S2

Time-lapse movie of the latex bead tracking analysis, related to Figure 3a, NT

MDCK cells were cultured on matrigel embedded with latex beads. Magenta spheres indicate the position of the latex beads and the green bar shows the beads' trajectories. In the movie, 1s = 75 min in real time. Bar = 50 μm.

Movie S3

Time-lapse movie of the latex bead tracking analysis, related to Figure 3a, Y-27632

The cells were treated with Y-27632 (10 ◎M). In the movie, 1s = 75 min in real time. Bar = 50 μm.

Movie S4

Time-lapse movie of the latex bead tracking analysis, related to Supplementary Figure 1a, NT-GP-Matrigel

MDCK cells were cultured on NT-GP-matrigel embedded with latex beads. Magenta spheres indicate the position of the latex beads, and the green bars show the beads' trajectories. In the movie, 1s = 75 min in real time. Bar = 50 μm.

Movie S5

Time-lapse movie of the latex bead tracking analysis, related to Supplementary Figure 1a, 0.25-GP-Matrigel

MDCK cells were cultured on 0.25-GP-matrigel embedded with latex beads. In the movie, 1s = 75 min in real time. Bar = 50 μm.

Movie S6

Time-lapse movie of the latex bead tracking analysis, related to Supplementary Figure 1a, 0.50-GP-Matrigel

MDCK cells were cultured on 0.50-GP-matrigel embedded with latex beads. In the movie, 1s = 75 min in real time. Bar = 50 μm.

References

1. Chauhan, B.K., Lou, M., Zheng, Y. & Lang, R.A. Balanced Rac1 and RhoA activities regulate cell shape and drive invagination morphogenesis in epithelia. *Proc Natl Acad Sci U S A* **108**, 18289-94 (2011).
2. Bonnans, C., Chou, J. & Werb, Z. Remodelling the extracellular matrix in development and disease. *Nat Rev Mol Cell Biol* **15**, 786-801 (2014).
3. Miner, J.H. & Yurchenco, P.D. Laminin functions in tissue morphogenesis. *Annu Rev Cell Dev Biol* **20**, 255-84 (2004).
4. Ogawa, T., Tsubota, Y., Hashimoto, J., Kariya, Y. & Miyazaki, K. The short arm of laminin gamma2 chain of laminin-5 (laminin-332) binds syndecan-1 and regulates cellular adhesion and migration by suppressing phosphorylation of integrin beta4 chain. *Mol Biol Cell* **18**, 1621-33 (2007).
5. Rozario, T. & DeSimone, D.W. The extracellular matrix in development and morphogenesis: a dynamic view. *Dev Biol* **341**, 126-40 (2010).
6. Lo, C.M., Wang, H.B., Dembo, M. & Wang, Y.L. Cell movement is guided by the rigidity of the substrate. *Biophys J* **79**, 144-52 (2000).
7. O'Brien, L.E., Zegers, M.M. & Mostov, K.E. Opinion: Building epithelial architecture: insights from three-dimensional culture models. *Nat Rev Mol Cell Biol* **3**, 531-7 (2002).
8. Haga, H., Irahara, C., Kobayashi, R., Nakagaki, T. & Kawabata, K. Collective movement of epithelial cells on a collagen gel substrate. *Biophys J* **88**, 2250-6 (2005).
9. Paszek, M.J. *et al.* Tensional homeostasis and the malignant phenotype. *Cancer Cell* **8**, 241-54 (2005).
10. Yeung, T. *et al.* Effects of substrate stiffness on cell morphology, cytoskeletal structure, and adhesion. *Cell Motil Cytoskeleton* **60**, 24-34 (2005).
11. Murrell, M., Kamm, R. & Matsudaira, P. Substrate viscosity enhances correlation in epithelial sheet movement. *Biophys J* **101**, 297-306 (2011).
12. Ishida, S. *et al.* Epithelial sheet folding induces lumen formation by Madin-Darby canine kidney cells in a collagen gel. *PLoS One* **9**, e99655 (2014).
13. Musah, S. *et al.* Substratum-induced differentiation of human pluripotent stem cells reveals the coactivator YAP is a potent regulator of neuronal specification. *Proc Natl Acad Sci U S A* **111**, 13805-10 (2014).
14. Fidler, A.L. *et al.* A unique covalent bond in basement membrane is a primordial innovation for tissue evolution. *Proc Natl Acad Sci U S A* **111**, 331-6 (2014).
15. Okuda, S., Inoue, Y., Eiraku, M., Adachi, T. & Sasai, Y. Vertex dynamics simulations

of viscosity-dependent deformation during tissue morphogenesis. *Biomech Model Mechanobiol* (2014).

16. Mizutani, T., Haga, H., Koyama, Y., Takahashi, M. & Kawabata, K. Diphosphorylation of the myosin regulatory light chain enhances the tension acting on stress fibers in fibroblasts. *J Cell Physiol* **209**, 726-31 (2006).
17. Ikebe, M., Hartshorne, D.J. & Elzinga, M. Identification, phosphorylation, and dephosphorylation of a second site for myosin light chain kinase on the 20,000-dalton light chain of smooth muscle myosin. *J Biol Chem* **261**, 36-9 (1986).
18. Matsui, T. *et al.* Rho-associated kinase, a novel serine/threonine kinase, as a putative target for small GTP binding protein Rho. *EMBO J* **15**, 2208-16 (1996).
19. Nishikawa, M., Tanaka, T. & Hidaka, H. Ca2+-calmodulin-dependent phosphorylation and platelet secretion. *Nature* **287**, 863-5 (1980).
20. Adelstein, R.S. & Conti, M.A. Phosphorylation of platelet myosin increases actin-activated myosin ATPase activity. *Nature* **256**, 597-8 (1975).
21. Lee, J.Y. & Harland, R.M. Actomyosin contractility and microtubules drive apical constriction in Xenopus bottle cells. *Dev Biol* **311**, 40-52 (2007).
22. Ivanov, A.I. *et al.* Myosin II regulates the shape of three-dimensional intestinal epithelial cysts. *J Cell Sci* **121**, 1803-14 (2008).
23. Martin, A.C. Pulsation and stabilization: contractile forces that underlie morphogenesis. *Dev Biol* **341**, 114-25 (2010).
24. Zhang, H. *et al.* A tension-induced mechanotransduction pathway promotes epithelial morphogenesis. *Nature* **471**, 99-103 (2011).
25. Dong, B., Deng, W. & Jiang, D. Distinct cytoskeleton populations and extensive crosstalk control Ciona notochord tubulogenesis. *Development* **138**, 1631-41 (2011).
26. Keller, R. Developmental biology. Physical biology returns to morphogenesis. *Science* **338**, 201-3 (2012).
27. Harding, M.J. & Nechiporuk, A.V. Fgfr-Ras-MAPK signaling is required for apical constriction via apical positioning of Rho-associated kinase during mechanosensory organ formation. *Development* **139**, 3130-5 (2012).
28. Vasquez, C.G., Tworoger, M. & Martin, A.C. Dynamic myosin phosphorylation regulates contractile pulses and tissue integrity during epithelial morphogenesis. *J Cell Biol* **206**, 435-50 (2014).
29. Huang, Y.C. *et al.* A natural compound (ginsenoside Re) isolated from Panax ginseng as a novel angiogenic agent for tissue regeneration. *Pharm Res* **22**, 636-46 (2005).
30. Sundararaghavan, H.G. *et al.* Genipin-induced changes in collagen gels: correlation of mechanical properties to fluorescence. *J Biomed Mater Res A* **87**, 308-20 (2008).

31. Yunoki, S., Ohyabu, Y. & Hatayama, H. Temperature-responsive gelation of type I collagen solutions involving fibril formation and genipin crosslinking as a potential injectable hydrogel. *Int J Biomater* **2013**, 620765 (2013).
32. Gao, L. *et al.* Effects of genipin cross-linking of chitosan hydrogels on cellular adhesion and viability. *Colloids Surf B Biointerfaces* **117**, 398-405 (2014).
33. Imai, M., Mizutani, T., Kawabata, K. & Haga, H. Secretion of different altered laminin isoforms results in three-dimensional morphological changes in cells cultured on Matrigel. in *2014 International Symposium on Micro-NanoMechatronics and Human Science (MHS)* p.p. 266-268 (Nagoya, Aichi, 2014).
34. Uehata, M. *et al.* Calcium sensitization of smooth muscle mediated by a Rho-associated protein kinase in hypertension. *Nature* **389**, 990-4 (1997).
35. Venn, G., Sims, T. & Mason, R.M. Collagen stability and cross-linking in normal and kyphoscoliotic mouse intervertebral discs. *Biosci Rep* **8**, 315-22 (1988).
36. Yang, Y.L. & Kaufman, L.J. Rheology and confocal reflectance microscopy as probes of mechanical properties and structure during collagen and collagen/hyaluronan self-assembly. *Biophys J* **96**, 1566-85 (2009).
37. LeBleu, V.S., Macdonald, B. & Kalluri, R. Structure and function of basement membranes. *Exp Biol Med (Maywood)* **232**, 1121-9 (2007).
38. Frantz, C., Stewart, K.M. & Weaver, V.M. The extracellular matrix at a glance. *J Cell Sci* **123**, 4195-200 (2010).
39. Hohenester, E. & Yurchenco, P.D. Laminins in basement membrane assembly. *Cell Adh Migr* **7**, 56-63 (2013).
40. Tan, W. & Desai, T.A. Layer-by-layer microfluidics for biomimetic three-dimensional structures. *Biomaterials* **25**, 1355-64 (2004).
41. Pelham, R.J. & Wang, Y. Cell locomotion and focal adhesions are regulated by substrate flexibility. *Proc Natl Acad Sci U S A* **94**, 13661-5 (1997).
42. Xu, B., Li, H. & Zhang, Y. An experimental and modeling study of the viscoelastic behavior of collagen gel. *J Biomech Eng* **135**, 54501 (2013).
43. Martín-Belmonte, F. *et al.* Cell-polarity dynamics controls the mechanism of lumen formation in epithelial morphogenesis. *Curr Biol* **18**, 507-13 (2008).
44. Guo, C.L. *et al.* Long-range mechanical force enables self-assembly of epithelial tubular patterns. *Proc Natl Acad Sci U S A* **109**, 5576-82 (2012).
45. Gildner, C.D., Roy, D.C., Farrar, C.S. & Hocking, D.C. Opposing effects of collagen I and vitronectin on fibronectin fibril structure and function. *Matrix Biol* **34**, 33-45 (2014).
46. Gutzman, J.H., Graeden, E.G., Lowery, L.A., Holley, H.S. & Sive, H. Formation of the

zebrafish midbrain-hindbrain boundary constriction requires laminin-dependent basal constriction. *Mech Dev* **125**, 974-83 (2008).

47. Martinez-Morales, J.R. *et al.* ojoplano-mediated basal constriction is essential for optic cup morphogenesis. *Development* **136**, 2165-75 (2009).
48. Nagase, K., Kobayashi, J. & Okano, T. Temperature-responsive intelligent interfaces for biomolecular separation and cell sheet engineering. *J R Soc Interface* **6 Suppl 3**, S293-309 (2009).
49. Tadakuma, K. *et al.* A device for the rapid transfer/transplantation of living cell sheets with the absence of cell damage. *Biomaterials* **34**, 9018-25 (2013).
50. Nam, E. *et al.* Comparison of the canine corneal epithelial cell sheets cultivated from limbal stem cells on canine amniotic membrane, atelocollagen gel, and temperature-responsive culture dish. *Vet Ophthalmol* (2014).

Acknowledgement

I would like to express the deepest appreciation to Prof. Hisashi Haga for his constructive comments and suggestion. Without face-to-face discussion with him, this thesis would not have been possible. His advices on both research as well as business manner have been priceless.

I would also like to thank Prof. Kazushige Kawabata and Assistant Prof. Takeomi Mizutani for insightful comment and practical advice. I am deeply grateful to Assistant Prof. Kazuya Furusawa for his crucial suggestion. My sincere thanks also go to Prof. Naoki Sasaki and Prof. Tokiyoshi Ayabe for reviewing this dissertation.

I thank members of the Laboratory of Cell Dynamics for their support in doing the experiments.

I would like to thank my parents Akira and Makiko Imai for financial support and moral help. My heartfelt appreciation goes to my husband, Kenji Takemoto, for his constant encouragements and emotional supports.